JM PAPERS

Influence of three-dimensionality on wake synchronisation of an oscillatory cylinder

Youngjae Kim[1],[†], Vedasri Godavarthi[1], Laura Victoria Rolandi[1], Joseph T. Klamo[2] and Kunihiko Taira[1]

[1]Department of Mechanical and Aerospace Engineering, University of California, Los Angeles, CA 90095, USA

[2]Systems Engineering Department, Naval Postgraduate School, Monterey, CA 93943, USA

We investigate the effect of three-dimensionality on the synchronisation characteristics of the wake behind an oscillating circular cylinder at $Re = 300$. Cylinder oscillations in rotation, transverse translation and streamwise translation are considered. We utilise phase-reduction analysis, which quantifies the phase-sensitivity function of periodic flows, to examine the synchronisation properties. Here, we present an ensemble-based framework for phase-reduction analysis to handle three-dimensional wakes that are not perfectly time-periodic. Based on the phase-sensitivity functions, synchronisability to three types of cylinder oscillations is evaluated. In spite of similar trends, we find that phase-sensitivity functions involving three-dimensional wakes are lower in magnitude compared with those of two-dimensional wakes, which leads to narrower conditions for synchronisation to weak cylinder oscillations. We unveil that the difference between the phase-sensitivity functions of two- and three-dimensional flows is strongly correlated to the amplitude variation of the three-dimensional flow by the cylinder motions. This finding reveals that the cylinder motion modifies the three-dimensionality of the wake as well as the phase of vortex shedding, which leads to reduced phase modulation. The synchronisation conditions of three-dimensional wakes, predicted by phase-reduction analysis, agree with the identification by parametric studies using direct numerical simulations for forced oscillations with small amplitudes. This study presents the potential capability of phase-reduction to study synchronisation characteristics of complex flows.

Key words: low-dimensional models, wakes

† Email address for correspondence: youngjaekim@ucla.edu

1001 A24-1

Y. Kim, V. Godavarthi, L.V. Rolandi, J.T. Klamo and K. Taira

1. Introduction

Synchronisation of the wake behind a bluff body to its structural vibration is of interest for various engineering applications. Such synchronisation can cause detrimental effects, such as structural fatigue and resonance induced by vortex-induced vibrations (Sarpkaya 2004; Williamson & Govardhan 2004). Alternatively, promoting synchronisation can enhance the performance in other engineering systems, such as the molecular mixing rate in chemical reactors (Celik & Beskok 2009), the heat transfer rate of heat exchangers (Gau, Wu & Su 2001) and the efficiency of energy-harvesting systems (Wang *et al.* 2020). The importance of accurately predicting synchronisation conditions in engineering systems cannot be emphasised enough (Bearman 1984; Naudascher & Rockwell 2005).

Previous studies have investigated the synchronisation between the vortex shedding frequency from a bluff body, mainly for a circular cylinder and its oscillatory motion. For various types of oscillation motions and Reynolds numbers, synchronisation regimes and vortex patterns have been identified and classified in both experimental and numerical studies (Olinger & Sreenivasan 1988; Ongoren & Rockwell 1988; Williamson & Roshko 1988; Woo 1999; Ponta & Aref 2005; Perdikaris, Kaiktsis & Triantafyllou 2009; Jacono *et al.* 2010; Leontini, Jacono & Thompson 2011). These studies are based on time-consuming sweeps of the parametric space in the amplitude-frequency domain using forced motion of a bluff body. Moreover, the synchronisation boundaries are identified differently depending on the identification criteria used (Kumar, Navrose & Mittal 2016) and the wake measurement location (Kumar *et al.* 2013). These subtle difficulties in the identification of precise synchronisation conditions, as well as a lack of understanding the underlying physics, highlight some weaknesses of previous experimental and numerical approaches. Therefore, a theoretical approach to investigate synchronisation is desirable.

The theoretical approach we consider is phase-reduction analysis, which describes the dynamics of high-dimensional periodic flows in terms of a single scalar variable 'phase'. Phase-reduction analysis has been applied to nonlinear oscillators in a wide range of studies, including those on biological rhythms (Winfree 1967; Shiogai, Stefanovska & McClintock 2010) and chemical oscillators (Kuramoto 2003; Pietras & Daffertshofer 2019). This technique enables us to examine synchronisation without extensive parametric sweeps by identifying the phase response of flows to external perturbations (Taira & Nakao 2018; Khodkar & Taira 2020; Khodkar, Klamo & Taira 2021; Loe *et al.* 2021). Furthermore, phase-reduction analysis has been used to guide flow control of periodic flows (Nair *et al.* 2021; Godavarthi, Kawamura & Taira 2023; Loe *et al.* 2023; Fukami, Nakao & Taira 2024). However, all previous applications of phase-reduction analysis were focused on two-dimensional periodic flows, even though synchronisation in real engineering systems often involves three-dimensional flows. The three-dimensionality of a flow creates added richness compared with its two-dimensional counterpart, which influences the synchronisation properties. Hence, it is important to identify the influence of three-dimensionality on synchronisation. However, the implementation of phase-reduction analysis is not straightforward for three-dimensional wakes since, generally, they are not perfectly periodic.

In this study, we examine the effect of three-dimensionality on the synchronisation of a cylinder's wake to the motion of the cylinder. We consider rotational, cross-flow translational and streamwise translational oscillations, which are the bases of in-plane cylinder oscillation. We extend the phase reduction analysis to characterise the perturbation dynamics of three-dimensional flows. Since the underlying three-dimensionality

adds fluctuations to the limit cycle, we leverage an ensemble-averaging technique to obtain mean responses of the three-dimensional wake.

This paper is organised as follows. Physical characteristics of three-dimensional wakes are presented in § 2. Fundamentals of phase-reduction analysis for periodic flows are introduced in § 3 with a new technique to measure the phase response of three-dimensional flows. The results of the present phase-reduction analysis are provided in § 4, revealing the influence of three-dimensionality within the flow on the synchronisation. Conclusions are offered in § 5.

2. Numerical simulation of cylinder wakes

2.1. *Problem description and numerical set-ups*

We consider two- and three-dimensional incompressible wakes past a circular cylinder using direct numerical simulations (DNS). The Reynolds number in this study is selected as $Re = U_\infty D/\nu = 300$, where U_∞ is the free-stream velocity, D is the diameter of the cylinder and ν is the kinematic viscosity. The Reynolds number is selected such that the cylinder wake develops three-dimensional structures, which is discussed in more detail in § 2.2. A finite-volume formulation (Ham & Iaccarino 2004; Ham, Mattsson & Iaccarino 2006) and a fractional-step method (Kim & Moin 1985) with second-order accuracy are adopted for spatial discretisation and time stepping, respectively. The computational domain is extended to $(x, y)/D \in [-20, 30] \times [-40, 40]$ from the centre of the cylinder shown in figure 1. To simulate the three-dimensional wake, the spanwise extension of the computational domain is set to $z/D \in [-2, 2]$ with the spanwise extent of the cylinder being $L_z/D = 4$, which allows us to capture the three-dimensional features related to mode A and mode B instabilities (Barkley & Henderson 1996). Structured grids are generated near the cylinder and in the downstream region with the uniform grid size $\Delta z/D = 0.05$ in the spanwise direction, which sufficiently resolves flow structures of mode A and B ($\lambda_A/D \approx 4$ and $\lambda_B/D \approx 0.8$). To reduce computational costs, hybrid-typed grids with approximately 0.1 million and 7.3 million volume cells are used for two- and three-dimensional wakes, respectively. Grid distributions in other directions are stretched to cluster cells near the cylinder surface. Far-field regions are discretised in an unstructured manner. The time step size of $U_\infty \Delta t/D = 0.005$ guarantees the Courant–Friedrichs–Lewy (CFL) number remains small, $U_\infty \Delta t/\Delta x < 1$, during computations.

For the DNS of the flow over a stationary cylinder, Dirichlet boundary conditions are given to the inlet boundary with the free-stream velocity $\boldsymbol{u} = (U_\infty, 0, 0)$ and the cylinder surface with $\boldsymbol{u} = \boldsymbol{0}$, respectively. The far-field boundary is prescribed with a Neumann condition of $\partial \boldsymbol{u}/\partial n = \boldsymbol{0}$. The periodic boundary condition is enforced in the spanwise direction, and a convective outlet condition is given to the outflow boundary. Our numerical solutions are validated through a comparison of the Strouhal number, St, the lift coefficient, C_L, and the drag coefficient, C_D, respectively, defined as

$$St = \frac{f_L D}{U_\infty}, \quad C_L = \frac{F_L}{\frac{1}{2}\rho U_\infty^2 D L_z}, \quad C_D = \frac{F_D}{\frac{1}{2}\rho U_\infty^2 D L_z}, \quad (2.1a\text{–}c)$$

where ρ denotes the fluid density, F_L and F_D represent the lift and drag acting on the cylinder and f_L is the frequency of the lift fluctuations that contains the maximum energy. Table 1 summarises the validation of the current simulation.

To measure the phase-response and identify the synchronisation boundaries of the cylinder wake, we introduce impulsive and oscillatory motion for the cylinder in the DNS. The motions of the cylinder are prescribed with the instantaneous translational
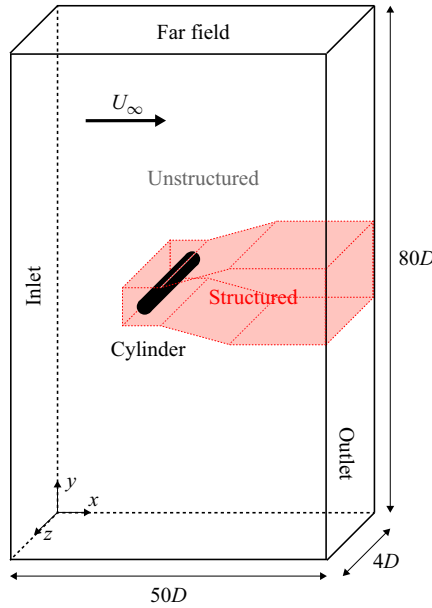
Y. Kim, V. Godavarthi, L.V. Rolandi, J.T. Klamo and K. Taira

Figure 1. Computational domain for DNS of three-dimensional cylinder wakes.

	St	C'_L	$\bar{C}_D$
Present (two-dimensional)	0.212	0.651	1.371
Zhang *et al.* (1995)	0.216	0.692	1.456
Persillon & Braza (1998)	0.209	0.526	1.405
Jiang *et al.* (2016)	0.211	0.641	1.377
Present (three-dimensional)	0.202	0.428	1.259
Zhang *et al.* (1995)	0.212	0.430	1.260
Persillon & Braza (1998)	0.206	0.477	1.366
Kravchenko, Moin & Shariff (1999)	0.203	0.400	1.280
Posdziech & Grundmann (2001)	0.201	0.410	1.250
Jiang *et al.* (2016)	0.204	0.464	1.296

Table 1. Comparison of the Strouhal number (St), root-mean-squared lift coefficient (C'_L) and time-averaged drag coefficients ($\bar{C}_D$) based on 200 shedding cycles for two- and three-dimensional cylinder flows at $Re = 300$.

or rotational speed of the cylinder, $U(t)$. The impulsive motion is approximated with a Gaussian function

$$U(t) = \varepsilon\delta(t - t_0) \simeq \frac{\varepsilon}{\sqrt{2\pi}\sigma} \exp\left[-\frac{1}{2}\left(\frac{t - t_0}{\sigma}\right)^2\right], \qquad (2.2)$$

where ε is the magnitude of the impulsive motion and σ determines the width of the Gaussian function, which is set to $\sigma = 10\Delta t$ in this study. Similarly, the oscillatory cylinder motion is modelled using the sinusoidal form

$$U(t) = U_f \sin(\Omega_f t), \qquad (2.3)$$

where U_f and Ω_f are the oscillation amplitude and angular frequency. Cylinder motions are incorporated in the DNS by modifying the boundary conditions depending on the type

of motion (Khodkar *et al.* 2021). For the rotating cylinder, $U(t)$ is assigned to the tangential velocity at the cylinder surface, replacing the no-slip condition. Cross-flow and streamwise translations are realised by moving the reference frame, subtracting $U(t)$ from the velocity at the inlet and far-field boundary.

2.2. *Wake characteristics of a stationary cylinder*

We analyse the fundamental flow physics of the three-dimensional wake of a stationary cylinder at $Re = 300$ focusing on its representation in the phase plane. We start by providing a definition of the phase, θ, and the amplitude, r, of a cylinder's wake based on the lift coefficient C_L and its Hilbert transform $\tilde{C}_L$ (Rosenblum, Pikovsky & Kurths 1996; Pikovsky *et al.* 1997) as

$$\theta(t) = \theta_0 + \tan^{-1} \frac{\tilde{C}_L(t)}{C_L(t)}, \quad r(t) = \sqrt{\tilde{C}_L(t)^2 + C_L(t)^2}, \qquad (2.4a,b)$$

$$\tilde{C}_L(t) = \frac{1}{\pi} \text{p.v.} \int_{-\infty}^{\infty} \frac{C_L(t)}{t - \tau} \, d\tau, \qquad (2.5)$$

where p.v. denotes the Cauchy principal value, and θ_0 is determined as $\pi/2$ to be consistent with earlier studies (Taira & Nakao 2018; Khodkar & Taira 2020).

The wake behind a circular cylinder undergoes the first bifurcation at $Re \approx 47$ caused by the primary instability. It triggers the wake transition from a flow with two steady counter-rotating vortices to a two-dimensional periodic flow with von Kármán vortex shedding (Jackson 1987; Provansal, Mathis & Boyer 1987). However, at $Re = 300$, since the computational domain is restricted to only be two-dimensional for the left-hand side graphic of figure 2(*a*), it qualitatively shows this primary instability. The two-dimensional wake presents a strong single peak in the corresponding frequency spectrum shown in figure 2(*c*), indicating the perfect periodicity of the two-dimensional wake. In the phase plane, the two-dimensional wake is represented by the limit cycle as shown in figure 2(*d*). By increasing the Reynolds number further, or in our case by making the computational domain three-dimensional in the case of the right-hand side graphic of figure 2(*a*), the second bifurcation occurs and the wake becomes three-dimensional. This transition to the three-dimensional flow is due to the emergence of two distinct instabilities (Williamson & Roshko 1988; Barkley & Henderson 1996; Williamson 1996; Posdziech & Grundmann 2001; Rolandi *et al.* 2023). The mode A instability occurs at $Re \approx 190$ with the spanwise wavelength $\lambda_A/D \approx 4$ which deforms the primary vortices. The mode B instability starts to appear at the higher Reynolds number of $Re \approx 240$ with the spanwise wavelength $\lambda_B/D \approx 0.8$. This instability mode is associated with secondary fine structures in the braid region, stretched in the streamwise direction and connecting the primary vortices. These instability modes create time-varying lift fluctuations associated with the more broadband frequency spectrum and a corresponding shift in the peak frequency, as shown in figure 2(*b*,*c*). The three-dimensional wake exhibits an unclosed trajectory with the amplitude variation in the phase plane, depicted in figure 2(*d*).

Two instantaneous flow snapshots corresponding to lower and higher amplitudes, $r = 0.44$ and 0.73, at the same phase, are visualised in figures 3(*a*) and 3(*b*), respectively. The visualisations distinctly emphasise the primary and secondary vortical structures by colouring the spanwise vorticity, ω_z, and streamwise vorticity, ω_x. We observe that the secondary vortical structures are more uniformly arranged and aligned with each other in the higher amplitude cycle with $r = 0.73$. Moreover, the primary vortices are more
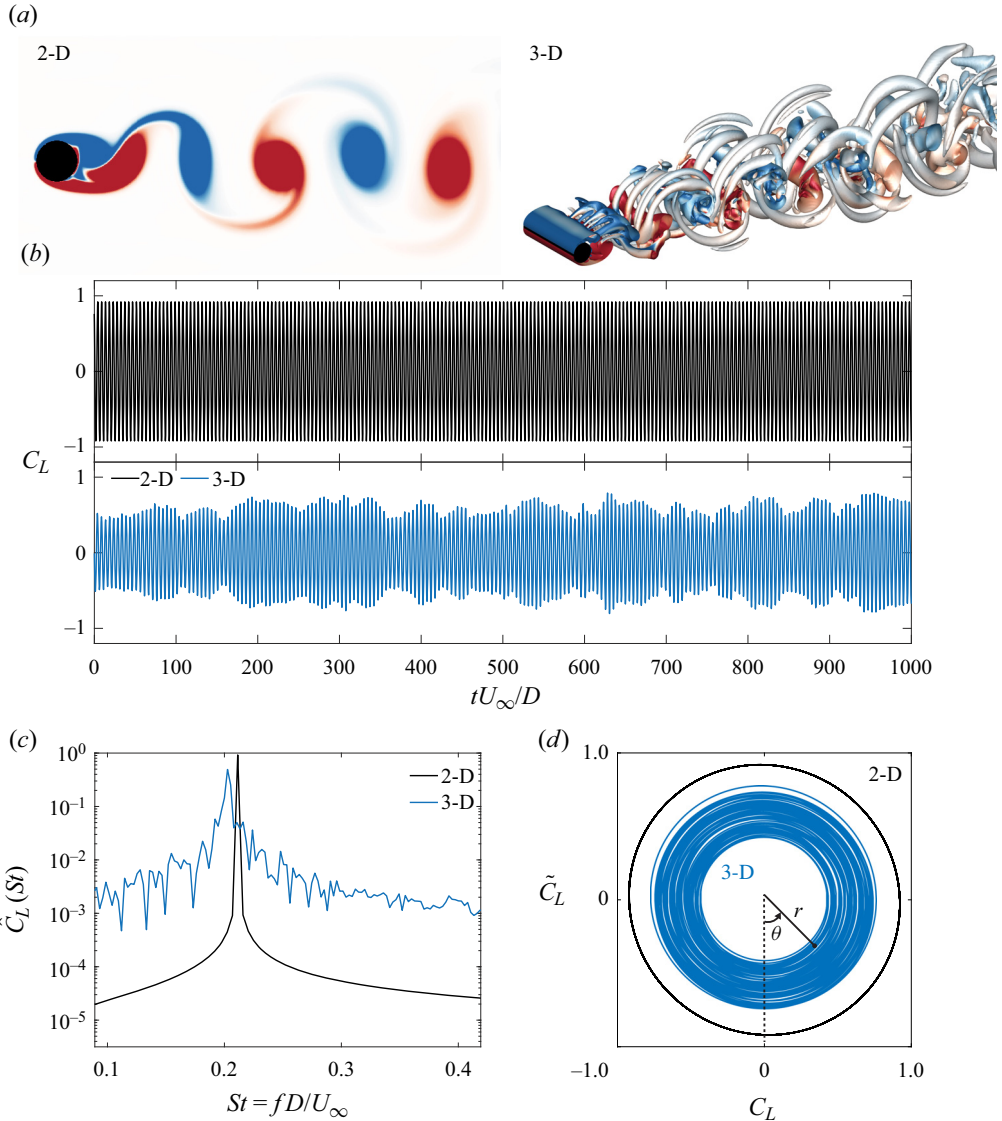
Figure 2. Comparison of two- and three-dimensional wakes at $Re = 300$. (*a*) Contours of spanwise vorticity of the two-dimensional wake and flow structures of three-dimensional wake visualised by the isosurface of the Q-criterion at $Q = 0.05$ coloured by spanwise vorticity. (*b*) Temporal variation of the lift coefficient, (*c*) power spectra, $\hat{C}_L$, of the lift coefficient and (*d*) phase plane representation of the lift coefficient.

coherent along the spanwise direction. In contrast, in the lower-amplitude cycle with $r = 0.44$, the streamwise stretched vortical structures appear less organised, and the primary vortex cores exhibit greater dislocations and deformation along the spanwise direction.

Similar trends are seen more clearly in scale-decomposed flow structures (Fujino, Motoori & Goto 2023). We apply a spatial band-pass filter to the velocity field based on a two-dimensional Gaussian kernel, G, in the x and y directions with the length scale
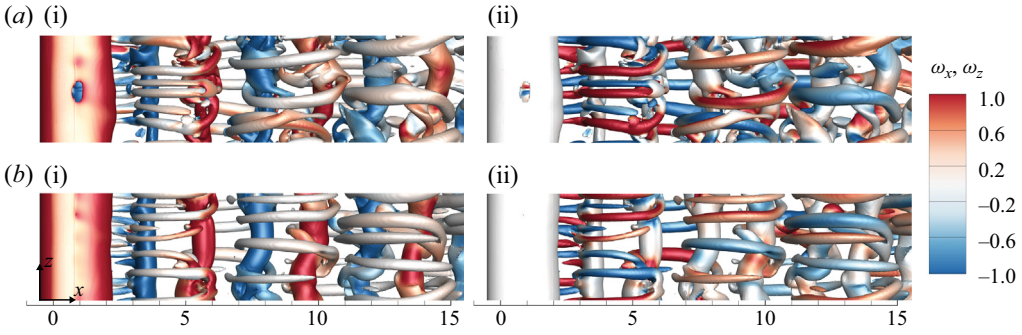
Figure 3. Instantaneous wake from a stationary cylinder visualised by isosurfaces of the Q-criterion ($Q = 0.05$) coloured with (i) ω_z and (ii) ω_x corresponding to (a) $r = 0.44$ and (b) 0.73.
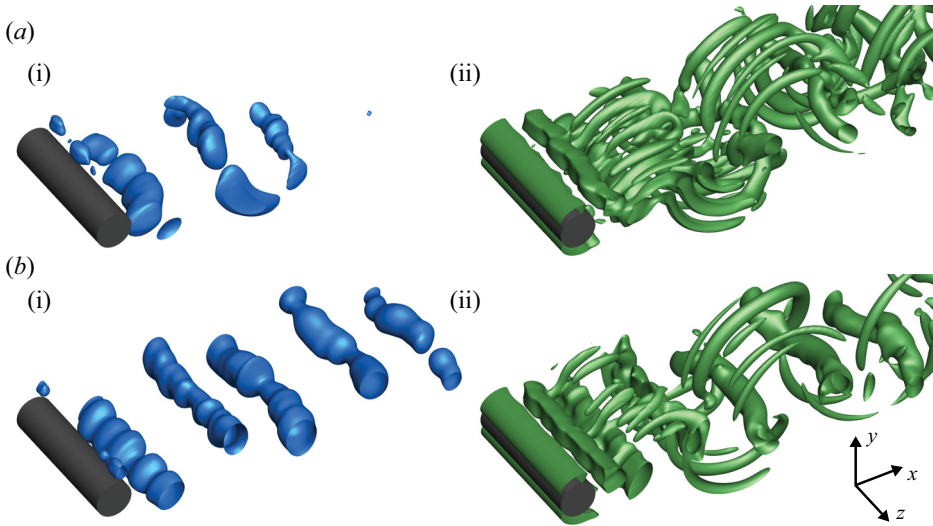

Figure 4. Instantaneous visualisation of scale-decomposed flows by isosurfaces of the Q-criterion ($Q = 0.05$) corresponding to (a) $r = 0.44$ and (b) 0.73. Panels (i) and (ii) capture large-scale $[\sigma_{max}, 2\sigma_{max}]$ and small-scale $[\sigma_{max}/4, \sigma_{max}/2]$ structures, respectively.

range of $[\sigma_1, \sigma_2]$ as

$$\boldsymbol{u}^{[\sigma_1, \sigma_2]}(x, y, z, t) = \int_{\mathcal{S}} \boldsymbol{u}(x, y, z, t) \left[G(x', y'; x, y, \sigma_1) - G(x', y'; x, y, \sigma_2) \right] \mathrm{d}x' \, \mathrm{d}y', \quad (2.6)$$

where

$$G(x', y'; x, y, \sigma) = \frac{1}{2\pi\sigma^2} \exp\left[-\frac{(x - x')^2 + (y - y')^2}{2\sigma^2} \right] \quad (2.7)$$

and the integration window $\mathcal{S}$ covers the whole computational domain in the x and y directions. Large- and small-scale flow structures with a length scale range of $[\sigma_{max}, 2\sigma_{max}]$ and $[\sigma_{max}/4, \sigma_{max}/2]$ are visualised in figure 4, where the cutoff length scale is $\sigma_{max} = D/(2\pi St)$ (Yasuda, Goto & Vassilicos 2020). We observe more large-scale structures as the amplitude r increases, whereas the small-scale structures diminish. These observations tell us that the cylinder wake is more irregular as the amplitude r decreases.
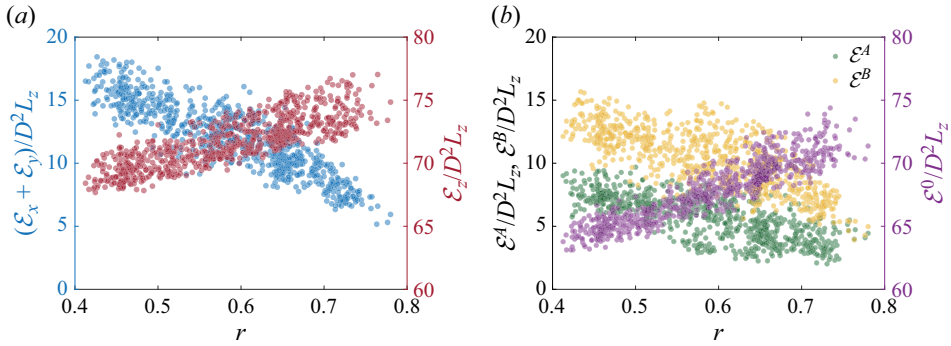
Figure 5. Variation of enstrophies with r. (a) Spanwise enstrophy $\mathcal{E}_z$ and non-spanwise enstrophy $\mathcal{E}_x + \mathcal{E}_y$. (b) Enstrophies of spanwise-averaged vorticity $\mathcal{E}^0$, mode A $\mathcal{E}^A$ and mode B $\mathcal{E}^B$.

These patterns can also be quantitatively identified by enstrophies defined as

$$\mathcal{E}_i = \int_{\mathcal{V}} \omega_i^2 \, d\mathbf{x}, \quad \mathcal{E} = \int_{\mathcal{V}} \boldsymbol{\omega} \cdot \boldsymbol{\omega} \, d\mathbf{x} = \mathcal{E}_x + \mathcal{E}_y + \mathcal{E}_z, \quad (2.8a,b)$$

where ω_i denotes the vorticity component in each direction ($i = x$, y and z). The non-spanwise enstrophy $\mathcal{E}_x + \mathcal{E}_y$ characterises the three-dimensionality of the wake induced by the spanwise mixing. The integration window $\mathcal{V}$ is set to $(x, y, z)/D \in [-1, 4] \times [-3, 3] \times [-2, 2]$ to examine flow structures formed within one shedding period. The variation in the non-spanwise enstrophy, $\mathcal{E}_x + \mathcal{E}_y$, and spanwise enstrophy, $\mathcal{E}_z$, with r is shown in figure 5(a). A decrease in r corresponds to a decrease in $\mathcal{E}_z$ and an increase in $\mathcal{E}_x + \mathcal{E}_y$. This indicates that larger spanwise mixing occurs when r is smaller and induces enhancement in three-dimensional flow structures. Moreover, weaker spanwise vortices are reflected as portions of smaller fluctuation amplitude in the C_L time history, which corresponds to smaller r in the phase plane.

To identify the dependencies between the instabilities and phase-amplitude variations of the three-dimensional wake, we apply the discrete Fourier transform (DFT) in the spanwise direction, which leads to the decomposition of the vorticity field as

$$\boldsymbol{\omega}(\mathbf{x}, t) = \sum_{m=0}^{N_z/2} \hat{\boldsymbol{\omega}}(x, y, t, m) e^{2\pi i m z/L_z} = \boldsymbol{\omega}^0(\mathbf{x}, t) + \boldsymbol{\omega}^A(\mathbf{x}, t) + \boldsymbol{\omega}^B(\mathbf{x}, t), \quad (2.9)$$

where $\hat{\boldsymbol{\omega}}$ denotes the coefficient of each Fourier mode and $N_z = L_z/\Delta z$ is the number of grid points in the spanwise direction. We categorise the Fourier modes into three vorticity components corresponding to the spanwise average ($\boldsymbol{\omega}^0$), mode A ($\boldsymbol{\omega}^A$) and mode B ($\boldsymbol{\omega}^B$). In other words, Fourier modes with large wavelengths, such that $\lambda/D \geq 2$, are considered mode A, and the remaining Fourier modes, with shorter wavelengths, are classified as mode B. This wavelength threshold is chosen to fall within a range of stable wavelengths that separate the range of unstable wavelengths of mode A and mode B (Leontini, Jacono & Thompson 2015; Rolandi *et al.* 2023).

As in the previous analysis, we quantify the contribution of each vorticity component by evaluating total enstrophy as shown in figure 5(b). Attributing to the orthogonality of Fourier modes, the total enstrophy, $\mathcal{E}$, is also decomposed into three parts as $\mathcal{E} = \mathcal{E}^0 + \mathcal{E}^A + \mathcal{E}^B$. Mode B surpasses mode A through the entire range of r, which implies the finer structures from the mode B instability are more prominent than large-scale structures from
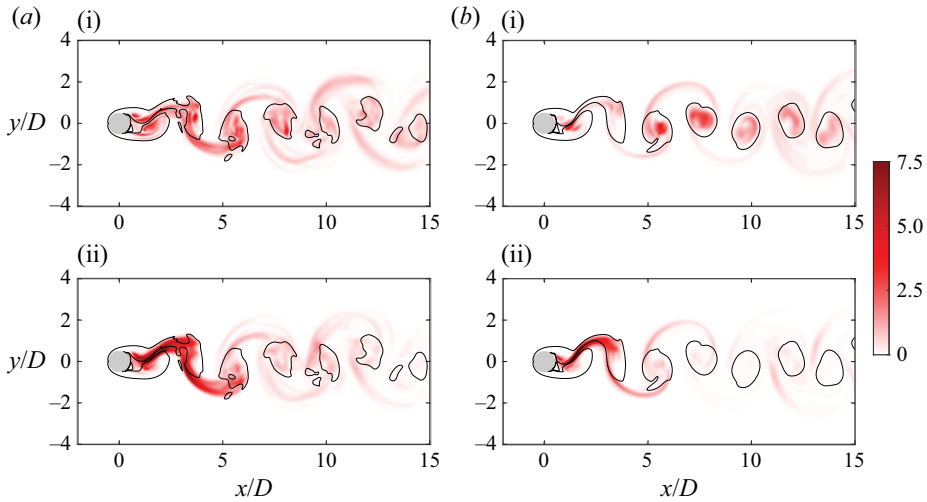
Figure 6. Contours of spanwise-averaged (i) $\boldsymbol{\omega}^A \cdot \boldsymbol{\omega}^A$ and (ii) $\boldsymbol{\omega}^B \cdot \boldsymbol{\omega}^B$ for (*a*) $r = 0.44$ and (*b*) 0.73. The black lines represent the contour lines of $\omega_z^0 = \pm 0.5$.

mode A. Both $\mathcal{E}^A$ and $\mathcal{E}^B$ become larger as r decreases, whereas $\mathcal{E}^0$ shows the opposite trend. Thus, it can be argued that secondary instabilities convert two-dimensional flow features in the wake to three-dimensional structures as r decreases.

We also identify regions where each instability mode actively grows by plotting the magnitudes of each vorticity component in figure 6. For the shedding cycle with $r = 0.73$, the mode A vorticity component highlights primary vortex cores, whereas mode B structures reside in the shear layers connecting two primary vortices. Flow structures of mode A last longer in the downstream region than mode B structures which implicates a faster decay rate of the mode B structures (Jiang *et al.* 2016). Moreover, smooth isocontour lines of ω_z^0 in figure 3(*b*) reflect the coherence of primary vortices in the spanwise direction. These trends are generally maintained in shedding cycles with smaller r, although the distributions of instability modes become more irregular due to the enhanced spanwise mixing. In particular, we observe that the mode A vorticity component at smaller r no longer only highlights primary vortex core regions but it is also present in the braid region. Flow structures associated with the mode B vorticity component are stronger and thickened in the braid regions, which gives rise to larger elongated vortical structures in this region. This can also be seen in figure 3. These originate from the thickening of the shear layers in the braid region connecting the two primary vortices, which now allows flow structures with the larger wavelength to be amplified within this region.

3. Phase-reduction analysis of fluid flows

3.1. *Phase-reduction analysis of periodic flows*

The dynamics of incompressible flows governed by the Navier–Stokes (NS) equations can be expressed with the state vector $\boldsymbol{q}$ and the NS operator $\mathcal{N}$ as

$$\frac{\partial}{\partial t}\boldsymbol{q}(\boldsymbol{x}, t) = \mathcal{N}(\boldsymbol{q}(\boldsymbol{x}, t)), \tag{3.1}$$

where $\boldsymbol{x}$ and t denote dimensionless space and time, respectively. A periodic flow can be described as a limit cycle solution $\boldsymbol{q}_0$ of the governing equation (3.1) with phase θ. Since

1001 A24-9

q_0 is periodic, $q_0(x, t) = q_0(x, t + 2\pi/\Omega_n)$ where Ω_n is the natural angular frequency of the flow. Here, we consider the phase functional $\Theta(q)$ that allows us to relate the high-dimensional instantaneous flow field q to its phase variable θ. The concept of phase, $\Theta(q)$, is then extended to the vicinity of the limit cycle to describe weakly perturbed flows. More specifically, if the flow $q(x, t)$ asymptotically converges to the limit cycle solution $q_0(x, t)$ as it develops, the phase of q is defined as $\Theta(q(x, t)) = \Theta(q_0(x, t))$. Combined with the governing equation (3.1), the phase dynamics of the unperturbed periodic flow can be described using functional derivatives of $\Theta(q)$ as

$$\dot{\theta} = \dot{\Theta}(q(x, t)) = \int_{\mathcal{V}_f} \frac{\delta\Theta}{\delta q} \cdot \dot{q} \, dx = \int_{\mathcal{V}_f} \frac{\delta\Theta}{\delta q} \cdot \mathcal{N}(q) \, dx = \Omega_n, \qquad (3.2)$$

where $\mathcal{V}_f$ denotes the control volume.

Now, suppose a small perturbation term, with magnitude $\varepsilon < 1$ and spatiotemporal profile $p(x, t)$ such that $\|p(x, t)\| = 1$, is added to (3.1) to analyse the dynamics of perturbed flows,

$$\frac{\partial}{\partial t}q(x, t) = \mathcal{N}(q(x, t)) + \varepsilon p(x, t). \qquad (3.3)$$

This leads to the phase dynamics of weakly perturbed flows,

$$\dot{\theta} = \int_{\mathcal{V}_f} \frac{\delta\Theta}{\delta q} \cdot (\mathcal{N}(q) + \varepsilon p(x, t)) \, dx = \Omega_n + \varepsilon \int_{\mathcal{V}_f} \frac{\delta\Theta}{\delta q} \cdot p(x, t) \, dx. \qquad (3.4)$$

For a weak perturbation, the functional derivative $\delta\Theta/\delta q$ can be linearly approximated with respect to the limit cycle $q = q_0$. This yields the spatial phase-sensitivity function

$$Z(x; \theta) \equiv \left. \frac{\delta\Theta(q)}{\delta q} \right|_{q=q_0}, \qquad (3.5)$$

which provides the linear phase response of fluid flows to small external perturbations. In particular, (3.4) is further simplified by introducing the phase-sensitivity function $\zeta(\theta)$ associated with the spatial forcing profile $f(x)$ as

$$\dot{\theta} = \Omega_n + \varepsilon\eta(t)\zeta(\theta), \quad \zeta(\theta) = \int_{\mathcal{V}_f} Z(x; \theta) \cdot f(x) \, dx, \qquad (3.6a,b)$$

when the perturbation can be decomposed as $p(x, t) = \eta(t)f(x)$.

Among the various approaches to determine the phase-sensitivity function $\zeta(\theta)$ (Nakao 2016; Iima 2019; Kawamura, Godavarthi & Taira 2022), we employ the direct method which can be performed in both numerical and experimental studies (Taira & Nakao 2018). For this method, a weak impulsive perturbation $\eta(t) = \delta(t - t_0)$ is applied to the flow at different phases, where $\delta(t - t_0)$ is a Dirac-delta function centred at $t = t_0$. When the transient effects of the impulsive perturbation settle, the perturbed flow returns to a stable state on the limit cycle, leaving an asymptotic phase shift. The asymptotic phase shift is often referred to as the phase-response function $g(\theta; \varepsilon) = \lim_{t\to\infty}[\Theta(q_\delta(x, t)) - \Theta(q_0(x, t))]$, where q_δ denotes the state vector of the flow perturbed impulsively at θ. The phase-sensitivity function, $\zeta(\theta)$, is calculated by integrating (3.6a,b) with an impulsive perturbation and results in $\zeta(\theta) \approx g(\theta; \varepsilon)/\varepsilon$ through the first-order approximation (Nakao 2016). Based on this perspective, the phase-sensitivity function can be interpreted physically as how much phase advancement, or delay, would be induced by imposing an external impulsive perturbation at a particular phase of the system.

Using (3.6*a*,*b*), the synchronisation of wake dynamics to any periodic forcing, with angular frequency Ω_f, can be investigated theoretically. Synchronisation between the flow and the periodic forcing is achieved when the relative phase $\phi(t) \equiv \theta(t) - \Omega_f t/m$ converges to a constant value, i.e.

$$\dot{\phi} = \Omega_n - \frac{\Omega_f}{m} + \varepsilon \eta(t) \zeta \left(\phi + \frac{\Omega_f}{m} t \right) \to 0, \tag{3.7}$$

where the natural number m denotes the subharmonic number of interest. This expression can be rewritten in an autonomous form by averaging over a period of the perturbation $T_f = 2\pi/\Omega_f$ (Kuramoto 2003; Ermentrout & Terman 2010),

$$\dot{\phi} \simeq \Omega_n - \frac{\Omega_f}{m} + \varepsilon \Gamma(\phi), \tag{3.8}$$

where $\Gamma(\phi)$ is the phase-coupling function given by

$$\Gamma(\phi) = \frac{1}{T_f} \int_{-\pi/\Omega_f}^{\pi/\Omega_f} \zeta \left(\phi + \frac{\Omega_f}{m} \tau \right) \eta(\tau) \, \mathrm{d}\tau = \frac{1}{2\pi} \int_{-\pi}^{\pi} \zeta \left(\phi + \frac{\varphi}{m} \right) \eta \left(\frac{\varphi}{\Omega_f} \right) \mathrm{d}\varphi. \tag{3.9}$$

Considering the stable solution of (3.8), the condition for synchronisation can be derived theoretically as

$$\varepsilon \min \Gamma(\phi) \leq \frac{\Omega_f}{m} - \Omega_n \leq \varepsilon \max \Gamma(\phi), \tag{3.10}$$

and the synchronisability is defined as $S = \max \Gamma - \min \Gamma$. The condition described by (3.10) theoretically identifies the possible combination map of the forcing angular frequency, Ω_f, and magnitude, ε, that can achieve synchronisation, known as the Arnold tongue. The synchronisability, S, conveys the ease by which synchronisation is achieved for a specific periodic perturbation at a different forcing frequency. A larger S indicates that a smaller motion is sufficient for the flow to be synchronised with external forcing at angular frequency Ω_f.

3.2. *Ensemble-based phase-reduction framework*

Strictly speaking, the phase-reduction framework is only valid for perfectly periodic flows. However, as discussed in § 2, three-dimensional flows do not exhibit perfect limit-cyclic behaviour which requires care when performing phase-reduction analysis. In recent years, a few studies have worked on extending the phase-reduction approach to chaotic oscillators (Josić & Mar 2001; Kurebayashi *et al.* 2012; Schwabedal *et al.* 2012; Imai, Suetani & Aoyagi 2022; Tönjes & Kori 2022). Inspired by these works, we extend the phase-based description to three-dimensional flows.

The phase dynamics of three-dimensional flows can be expressed as

$$\dot{\theta} = \int_{\mathcal{V}_f} \frac{\delta \Theta}{\delta \boldsymbol{q}} \cdot \boldsymbol{\mathcal{N}}(\boldsymbol{q}) \, \mathrm{d}\boldsymbol{x} = \Omega_n + F(\boldsymbol{q}(\boldsymbol{x}, t)), \quad \int_{-\infty}^{\infty} F(\boldsymbol{q}(\boldsymbol{x}, t)) \, \mathrm{d}t = 0, \tag{3.11a,b}$$

where the term $F(\boldsymbol{q}(\boldsymbol{x}, t))$ represents the instantaneous frequency fluctuation from the natural angular frequency Ω_n, which stems from the phase diffusion of systems (Josić

& Mar 2001; Kurebayashi *et al.* 2012). Following the same procedure provided in § 3.1, the phase dynamics of the weakly perturbed three-dimensional flows are modelled as

$$\dot{\theta} = \Omega_n + F(\boldsymbol{q}(\boldsymbol{x}, t)) + \varepsilon \int_{\mathcal{V}_f} \frac{\delta \Theta}{\delta \boldsymbol{q}} \cdot \boldsymbol{p}(\boldsymbol{x}, t) \, \mathrm{d}\boldsymbol{x}. \tag{3.12}$$

Since we are more interested in the long-term dynamics when investigating synchronisation, observing the mean phase dynamics of the flow is more valuable than the instantaneous dynamics. Hence, we apply an ensemble-averaging to (3.12) which can be expressed as

$$\langle X \rangle = \lim_{K \to \infty} \frac{1}{K} \sum_{k=1}^{K} X^{(k)}, \tag{3.13}$$

where $\langle \cdot \rangle$ denotes the ensemble-averaging operator and $X^{(k)}$ is the kth realisation of a variable X. This yields

$$\langle \dot{\theta} \rangle = \Omega_n + \varepsilon \int_{\mathcal{V}_f} \left\langle \frac{\delta \Theta}{\delta \boldsymbol{q}} \right\rangle \cdot \boldsymbol{p}(\boldsymbol{x}, t) \, \mathrm{d}\boldsymbol{x}, \tag{3.14}$$

which has the same form as (3.4). Thus, we define the spatial phase-sensitivity function of three-dimensional flows as

$$\boldsymbol{Z}(\boldsymbol{x}; \theta) = \left\langle \left. \frac{\delta \Theta(\boldsymbol{q})}{\delta \boldsymbol{q}} \right|_{\boldsymbol{q}=\boldsymbol{q}_0} \right\rangle, \tag{3.15}$$

which evaluates $\langle \delta \Theta / \delta \boldsymbol{q} \rangle$ from (3.14) with respect to the unperturbed flow $\boldsymbol{q}_0(\boldsymbol{x}, t)$. We then obtain the phase-sensitivity function $\zeta(\theta)$ of three-dimensional flows for a given spatial forcing profile $\boldsymbol{f}(\boldsymbol{x})$ according to (3.6*a,b*). This leads us to the identical formulation of phase-coupling functions and synchronisation conditions provided in (3.9) and 3.10 for three-dimensional flows.

For practical implementation of the ensemble-based framework, we consider a finite number of sample cycles to estimate the phase-sensitivity function. We note that sample cycles are extracted based on the observed probabilistic distribution of their occurrence in three-dimensional flows to avoid biased sampling. In this study, since the amplitude variable, r, in the phase plane captures the three-dimensionality of the cylinder wake, we construct the probability density function of this cycle amplitude using a kernel density estimation with the Gaussian function (Bowman & Azzalini 1997) as shown in figure 7(*a*). We then divide $P(r)$ into subdivisions that have an equal probability, and sample cycles are extracted from each subdivision. We then apply the direct method to obtain the phase-response functions on these selected samples. Extracted sample cycles are perturbed impulsively at various phases to measure the phase-response function as shown in figure 8(*a*). Finally, the phase-sensitivity function is calculated by averaging and normalising with the impulse magnitude, ε, yielding

$$\zeta(\theta) \approx \frac{1}{\varepsilon K} \sum_{k=1}^{K} g^{(k)}(\theta; \varepsilon), \tag{3.16}$$

where $g^{(k)}(\theta; \varepsilon)$ denotes the phase-response function of the kth sample cycle from among a total of K cycles.
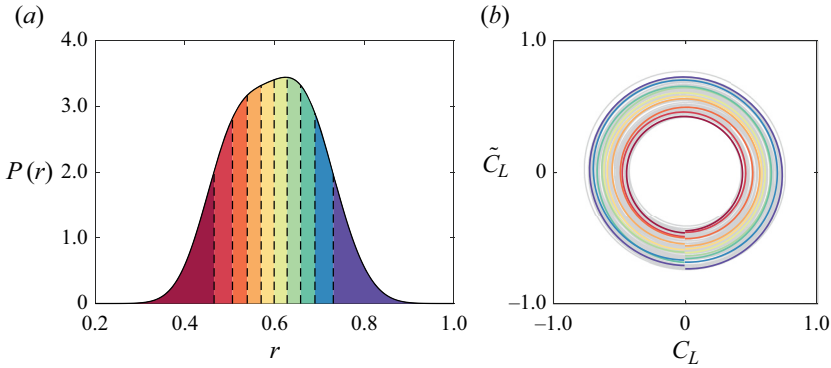
Figure 7. (*a*) Probability density function of cycle amplitude *r* for extraction and (*b*) 10 selected sample cycles.
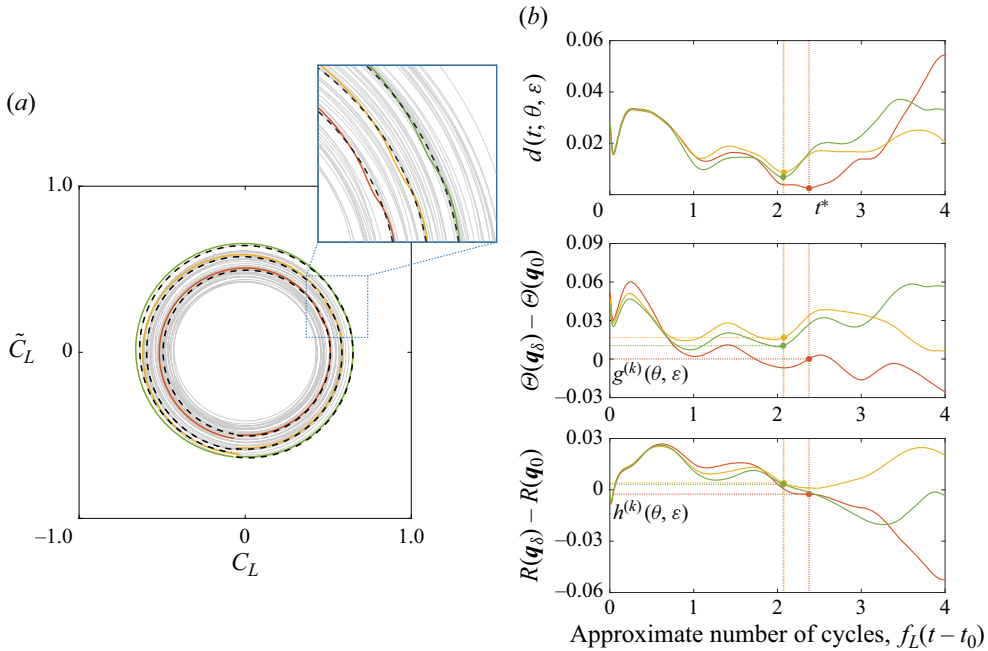

Figure 8. (*a*) Representation in the phase plane of three sample cycles, each with different amplitudes, perturbed at $\theta = 0.6\pi$ with rotary impulsive cylinder motion (solid) and the corresponding unperturbed sample cycles (dashed). (*b*) Estimation of $g^{(k)}(\theta, \varepsilon)$ and $h^{(k)}(\theta, \varepsilon)$ for ensemble-based phase-reduction analysis.

Determination of the phase-response function poses another challenge in the phase-reduction analysis of three-dimensional flows. Unlike for two-dimensional flows, the perturbed three-dimensional flow does not exactly return to the unperturbed trajectory due to its chaotic nature negating the concept of an asymptotic phase shift. This requires careful assessment of the phase-response function. We observe that when the perturbation is sufficiently weak, there exists a finite time interval where the dynamics of the perturbed flow remain analogous to the unperturbed flow. Within this finite time interval, the perturbed flow initially deviates from the unperturbed flow due to the transient effect of the perturbation. The perturbed flow then approaches the unperturbed flow on the phase

1001 A24-13

plane as the transient effect of the perturbation dies out. After this time horizon, the perturbed flow starts to deviate again from the unperturbed flow due to the chaotic nature of three-dimensional flows.

Based on this perspective, we use the time t^*, when the perturbed flow is closest to the unperturbed flow, to estimate the phase-response functions of three-dimensional flows. To determine t^*, we monitor the distance function d between the unperturbed and perturbed flows on the phase plane as shown in figure 8(*b*), which is defined as

$$d^{(k)}(t; \theta, \varepsilon) = \left[\left(R(\boldsymbol{q}_\delta^{(k)}) \right)^2 + \left(R(\boldsymbol{q}_0^{(k)}) \right)^2 - 2R(\boldsymbol{q}_\delta^{(k)}) R(\boldsymbol{q}_0^{(k)}) \cos \left(\Theta(\boldsymbol{q}_\delta^{(k)}) - \Theta(\boldsymbol{q}_0^{(k)}) \right) \right]^{1/2}$$

(3.17)

using the law of cosines. Similar to the way we denote the phase functional Θ as returning the phase $\theta(t) = \Theta(\boldsymbol{q}(\boldsymbol{x}, t))$ for a particular flow $\boldsymbol{q}(\boldsymbol{x}, t)$, the amplitude functional R returns the amplitude of that flow field as $r(t) = R(\boldsymbol{q}(\boldsymbol{x}, t))$. We now seek the time t^* such that d is minimised after the impulse perturbation and before it starts to grow again. To not be affected by the local fluctuations of d, we mainly track the variation of local minimum and maximum values of d. Both local maximum and minimum values of the distance function d keep decreasing as the transient effects of the perturbation diminish. When either the local minimum or maximum value of d increases, we can presume that the perturbed flow has started to deviate from the unperturbed flow. Thus, we take the time t^* to be when we observe the minimum value in the function d before either of the extrema values start to increase. Finally, the phase-response function is measured as $g^{(k)}(\theta; \varepsilon) = \Theta(\boldsymbol{q}_\delta^{(k)}(\boldsymbol{x}, t^*)) - \Theta(\boldsymbol{q}_0^{(k)}(\boldsymbol{x}, t^*))$ for each sample cycle, as shown in figure 8(*b*).

In addition to the phase-response and phase-sensitivity functions, we can similarly measure the amplitude variation introduced by the weak impulsive perturbation. Since r denotes the three-dimensional characteristics of the wake, the deviation of the amplitude in the phase plane trajectory at t^* represents a modification of underlying three-dimensional characteristics. In this context, we also quantify the function $h^{(k)}(\theta; \varepsilon) = R(\boldsymbol{q}_\delta^{(k)}(\boldsymbol{x}, t^*)) - R(\boldsymbol{q}_0^{(k)}(\boldsymbol{x}, t^*))$ in addition to the phase-response functions as shown in figure 8(*b*). Similar to the phase-sensitivity function $\zeta(\theta)$, the function h is averaged and normalised with the impulse magnitude, ε, to give the function $\xi(\theta)$ defined as

$$\xi(\theta) \equiv \frac{1}{\varepsilon K} \sum_{k=1}^{K} h^{(k)}(\theta; \varepsilon).$$

(3.18)

This function represents the mean normalised variation of r made by the impulsive perturbations.

4. Synchronisation characteristics of three-dimensional wake

Let us numerically investigate the synchronisation between oscillations of a circular cylinder and its wake based on phase-reduction analysis. In order to study the influence of the three-dimensionality in the wake, we compare the three-dimensional wake synchronisation characteristics with the imposed two-dimensional wake ones at the same Reynolds number. As mentioned in § 1, we consider three types of in-plane cylinder motions, streamwise translation, cross-flow translation and rotation. While the two-dimensional wake is analysed as presented in § 3.1, the three-dimensional wake is studied using the ensemble-based phase-reduction analysis with 10 sample cycles as
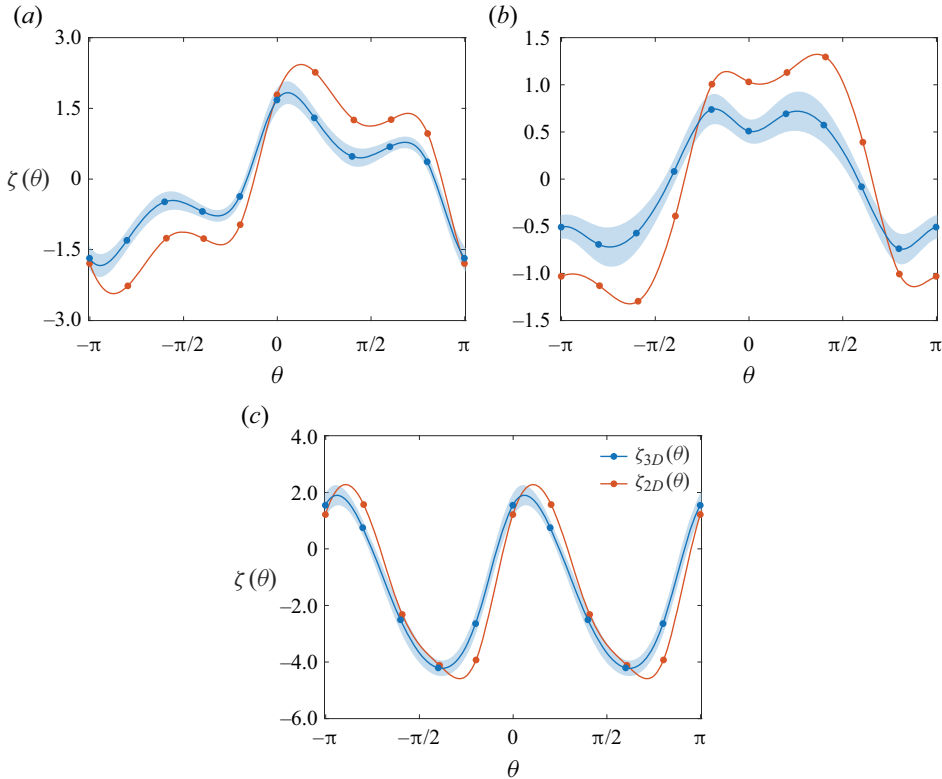
Figure 9. Comparison of phase-sensitivity functions of two- and three-dimensional wakes, denoted as $\zeta_{2D}(\theta)$ and $\zeta_{3D}(\theta)$ respectively, at $Re = 300$ for each perturbation type: (*a*) rotary, (*b*) cross-flow and (*c*) streamwise. The shaded area displays the 95 % confidence interval of $\zeta_{3D}(\theta)$.

shown in figure 7(*b*). The sample cycles are extracted based on the probability density function constructed with 200 shedding cycles provided in figure 7(*a*), which is identified to be of sufficient length for the convergence of the cumulative distribution function. We apply the impulsive cylinder motion with a magnitude of $\varepsilon/U_\infty = 0.025$, which is identified as being sufficiently small to satisfy the linearity assumption, to measure the phase-sensitivity functions. This identification is performed by testing successively smaller impulse magnitudes and noting that corresponding decreases occurred in the phase or amplitude difference between the perturbed and unperturbed flows. However, decreasing the impulse magnitude from 0.025 to 0.0125 does not produce meaningful changes in the phase or amplitude difference for either of the three types of motions used.

Two- and three-dimensional wake phase-sensitivity functions for rotary, cross-flow translation and streamwise translation motions are compared in figure 9. The ensemble-averaged $\zeta(\theta)$ for three-dimensional flows are shown in blue and the light blue regions show the 95 % confidence intervals obtained from the samples. We note that the overall trend of three-dimensional wake phase-sensitivity functions resembles those from two-dimensional wakes. This is because the two-dimensional coherent structures in von Kármán vortex shedding are predominant, even in three-dimensional wakes at $Re = 300$, over the secondary instabilities. Hence, the perturbation dynamics of the flow follow the shedding of spanwise vortices. This implies that the potential exists to use two-dimensional flows from low to moderate Reynolds numbers to capture phase-sensitivity functions
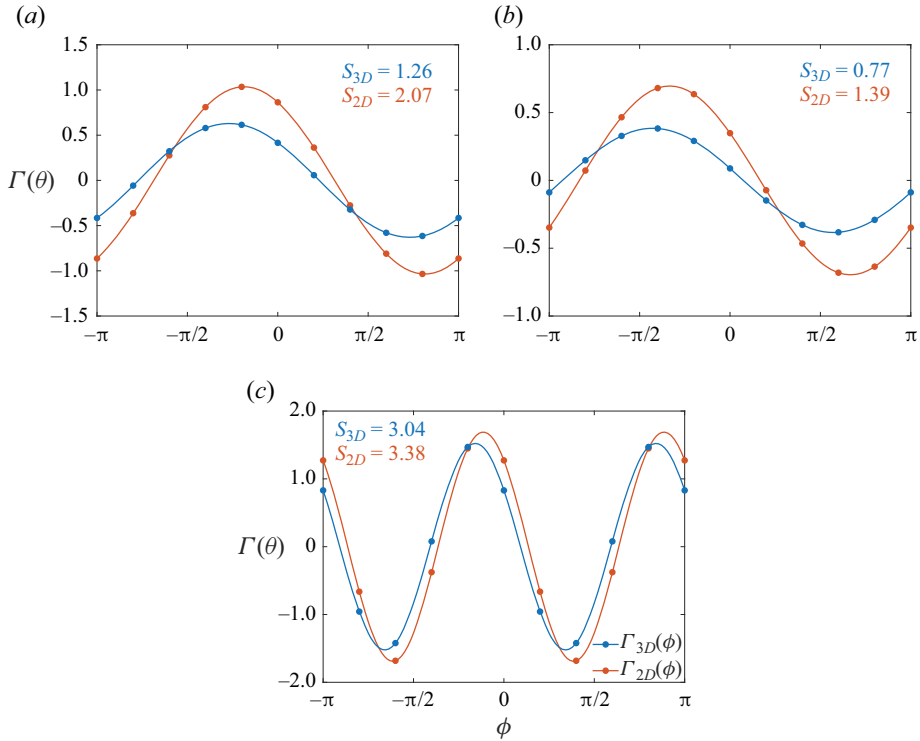
Figure 10. Phase-coupling functions, $\Gamma_{2D}(\phi)$ and $\Gamma_{3D}(\phi)$, and synchronisability, S_{2D} and S_{3D}, evaluation of two- and three-dimensional wakes for each perturbation type: (*a*) rotary; (*b*) cross-flow; (*c*) streamwise.

and perturbation dynamics for three-dimensional flows at the equivalent Reynolds number.

We find that the three-dimensional wake is less sensitive than the two-dimensional wake to all three types of external perturbation in terms of the phase. The magnitudes of the phase-sensitivity functions for a three-dimensional wake are decreased significantly for the rotary and cross-flow perturbations. In contrast, the phase-sensitivity function for the streamwise perturbation is much less affected by the three-dimensionality. When the cylinder translates in the streamwise direction, it moves towards or away from the vortices behind it. Thus, a phase shift by the streamwise motion is largely associated with the adjustment of distance between the cylinder and the spanwise vortices. This distance is less affected by the spanwise three-dimensionality of the wake.

Using the phase-sensitivity functions, we determine the synchronisability of the wake to steady sinusoidal oscillations using the phase-coupling functions, $\Gamma(\phi)$. Phase-coupling functions of two- and three-dimensional wakes are evaluated and shown in figure 10. Since the synchronisation of the cylinder wake to streamwise oscillations mainly occurs when $\Omega_f \approx 2\Omega_n$ (Al-Mdallal, Lawrence & Kocabiyik 2007; Marzouk & Nayfeh 2009), the second harmonic ($m = 2$) is investigated for the streamwise translation. In fact, the phase coupling function with $m = 1$ for streamwise oscillations is zero valued ($\Gamma(\phi) = 0$) due to the π periodicity of the phase-sensitivity function as shown in figure 9, indicating that synchronisation to the first harmonic is hardly seen. However, synchronisation to the first harmonic of streamwise cylinder oscillations can occur for large enough
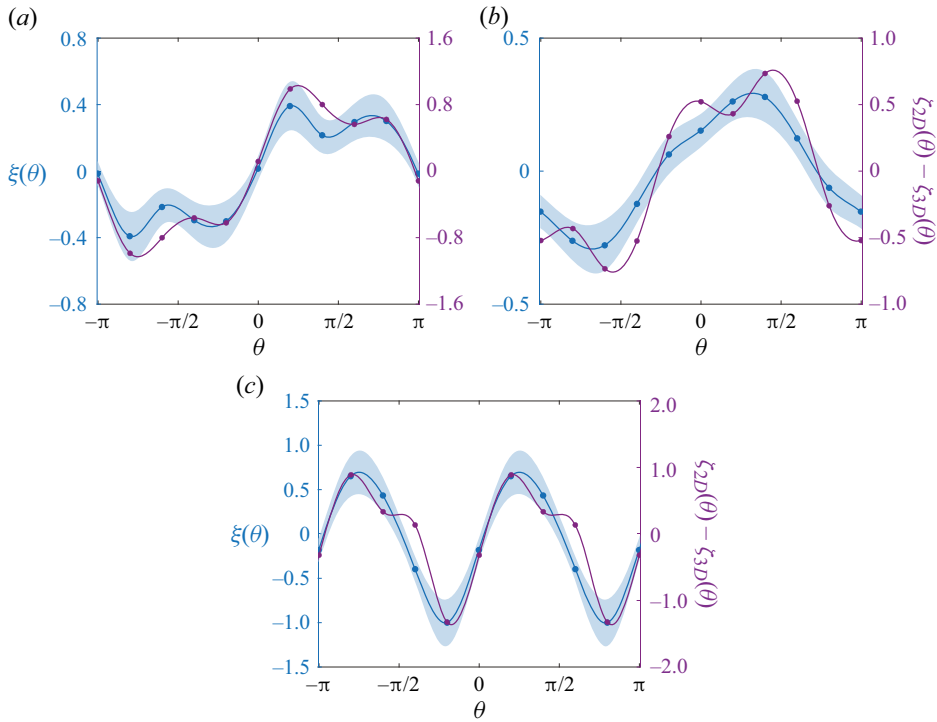
1001 A24-16

Figure 11. Amplitude variation, $\xi(\theta)$, for three-dimensional wakes normalised by the magnitude of impulsive cylinder motion along with 95 % confidence intervals: (*a*) rotary; (*b*) cross-flow; (*c*) streamwise. Differences between the phase-sensitivity functions of two- and three-dimensional wakes, $\zeta_{2D}(\theta) - \zeta_{3D}(\theta)$, are also provided for comparison.

oscillation amplitudes (Leontini, Jacono & Thompson 2013; Konstantinidis & Bouris 2016).

On the other hand, the first harmonic ($m = 1$) is targeted for rotation and cross-flow translation. Similar to the phase-sensitivity function results, we again observe that three-dimensionality within the wake imposes a higher resistance to synchronisation. Synchronisability to rotary and cross-flow oscillations shows a large reduction (39.1 % and 44.6 %, respectively) compared with the two-dimensional flow. The synchronisability to streamwise oscillation showed only a 10.1 % decrease.

To understand the source of the difference between the phase-sensitivity functions of two- and three-dimensional wakes at the same Reynolds number, we consider the effect of impulsive cylinder motion in an additional degree of freedom of the three-dimensional wake, the amplitude r. We compare $\xi(\theta)$ with the difference in phase sensitivities, $\zeta_{2D}(\theta) - \zeta_{3D}(\theta)$, for the three perturbation motions as shown in figure 11. We observe that the function $\xi(\theta)$ generally becomes larger at phases where the phase-sensitivity function of the three-dimensional wake exhibits a relatively large difference from the corresponding two-dimensional one. Correlation coefficients, ρ, between $\xi(\theta)$ and $\zeta_{2D}(\theta) - \zeta_{3D}(\theta)$ are also evaluated and have values higher than 0.9. This indicates that the energy given by the cylinder motion changes both the instantaneous phase and the amplitude in the phase plane. Recalling that the amplitude variable r reflects the instantaneous three-dimensional properties of the wake, it can be argued that the portion of energy transferred, in the amplitude direction, from the cylinder to the wake modifies the three-dimensional
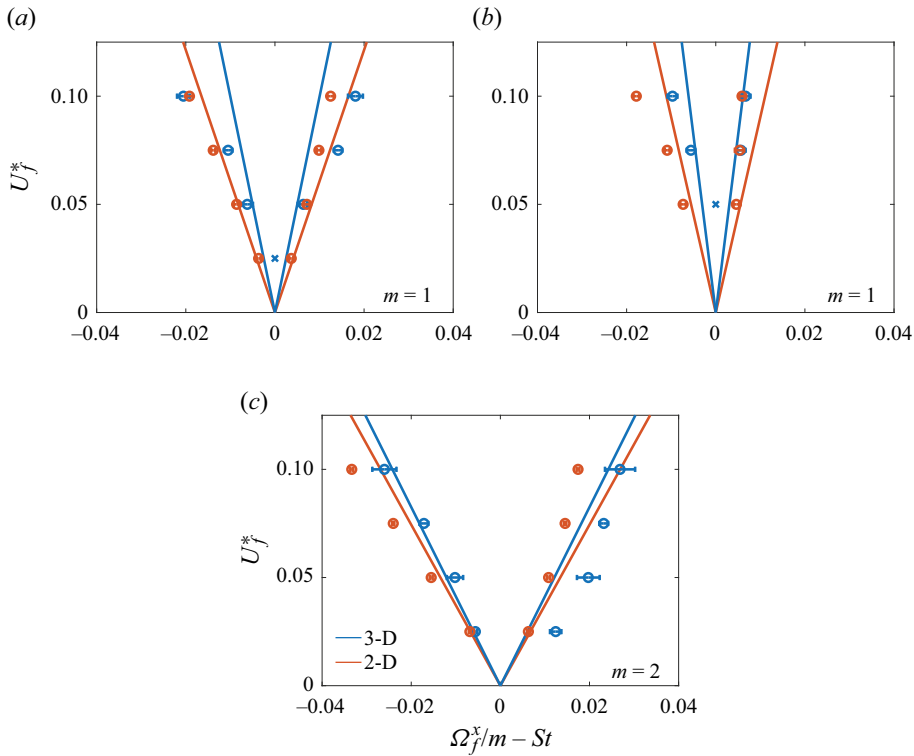
Figure 12. Synchronisation condition (Arnold tongue) for each type of oscillation motion predicted using phase-reduction analysis (solid lines) and identified using DNS (circles): (*a*) rotary; (*b*) cross-flow; (*c*) streamwise. Horizontal bars represent the uncertainty in the identification of synchronisation boundaries by DNS.

characteristics of the flow. However, since only the energy transferred in the instantaneous phase direction supports synchronisation, three-dimensional wakes require larger energy to achieve synchronisation as observed in the synchronisability estimations.

Based on (3.10), the synchronisation conditions of the non-dimensional forcing amplitude, $U_f^* = U_f/U_\infty$, and frequency, $\Omega_f^* = \Omega_f D/(2\pi U_\infty)$, can be theoretically predicted based on the phase-coupling functions and shown in figure 12. We validate our methodology and results by comparing the predicted synchronisation boundaries from phase-reduction analysis to DNS parametric studies. The region between the solid lines is predicted to be synchronised to the external forcing while the two regions outside the lines are predicted to be asynchronous. The circles indicate the synchronisation bounds determined by performing DNS with the cylinder undergoing steady and continuous oscillations at the corresponding forcing amplitude and frequency. Horizontal error bars represent the uncertainty in the identification of synchronisation boundaries associated with the nonuniform and finite resolution of the DNS parametric sweeps. Synchronisation in DNS is determined by monitoring the temporal variation of the phase difference, $\phi(t)$, between the sinusoidally forced cylinder oscillation and the wake, defined in (3.7). When $\phi(t)$ converges to a certain value with a small standard deviation, $\sigma(\phi(t)) < 0.1\pi$, we classify the case as synchronised.

From figure 12, we observe that phase-reduction analysis is able to predict the synchronisation conditions for both two- and three-dimensional wakes for $U_f^* < 0.1$,

1001 A24-18

indicating that the linear assumption is valid for oscillations with small amplitudes. As the oscillation amplitude of the non-dimensional velocity increases, the DNS results deviate from the predictions due to the stronger nonlinearity. In addition, synchronisation to rotary and cross-flow oscillations are not observed when the oscillation amplitude is weak, classified as $U_f^* = 0.025$ and 0.05 for each type of motion, respectively, and denoted as cross- symbols in the figure. As discussed in Pikovsky *et al.* (1997), chaotic oscillators with phase diffusion do not show synchronisation when the oscillation is not strong enough to suppress the phase diffusion.

To elaborate on this point theoretically, we look into the temporal variation of the instantaneous phase difference $\phi(t)$, which can be expressed approximately as

$$\dot{\phi}(t) \simeq \left(\Omega_n - \frac{\Omega_f}{m} \right) + F(\boldsymbol{q}(\boldsymbol{x}, t)) + U_f^* \eta(t) \zeta \left(\phi + \frac{\Omega_f}{m} t \right) \tag{4.1}$$

derived from (3.12). Let us now compare the scales of each term on the right-hand side of this equation under the assumption that the oscillation amplitude, U_f^*, is small and approaches zero. Since Ω_f/m should be very close to Ω_n to synchronise the wake to small-amplitude oscillations, the first term is negligible. The third term is also negligible because of the linear proportionality to U_f^*. However, the second term F is independent of the external forcing because it is an inherent property of the three-dimensional wake. Thus, the first and third terms disappear for small-amplitude oscillation conditions, and the dynamics of ϕ are governed predominantly by F as $\dot{\phi}(t) \simeq F(\boldsymbol{q}(\boldsymbol{x}, t))$. As a result, if instantaneous fluctuations F in three-dimensional flows are not sufficiently small, it prevents the convergence of ϕ unless F is restrained by relatively large oscillations. Thus, the oscillation amplitude has to exceed a certain threshold to facilitate synchronisation regardless of the forcing frequency. Furthermore, the third term is also proportional to the phase-sensitivity function, which implies a larger threshold for U_f^* when the magnitude of the phase-sensitivity function $\zeta(\theta)$ is smaller. This is seen in the largest threshold for U_f^* for the cross-flow oscillation and no threshold appearing within $U_f^* \geq 0.025$ for the streamwise oscillation, which correspond to the smallest and largest phase-sensitivity function magnitudes among oscillation types as shown in figure 9.

We also note that the left synchronisation boundaries obtained from the three-dimensional wake DNS results are located inside the two-dimensional wake results. This indicates the added difficulty in synchronising the three-dimensional wake as predicted by phase-reduction analysis. On the other hand, the right synchronisation boundaries, representing high-frequency oscillations, exhibit different trends depending on the oscillation type which deviates from the theoretical predictions.

For two-dimensional wakes, we commonly see deviations of the DNS identified right boundaries from the predictions by phase-reduction analysis, which is also observed in the previous study of Khodkar *et al.* (2021). They identified that synchronisation to higher frequencies is more restrictive than lower frequencies, attributing it to the physical constraint of the vortex formation region behind the cylinder. Synchronisation to high-frequency oscillations requires the vortex formation region to be compact. However, it is impossible to shorten the vortex formation region beyond a certain limit. This is reflected in the asymmetry of the DNS-based Arnold tongue and its inward deflection at the right branch for two-dimensional wakes. This hypothesis, however, only applies to two-dimensional wakes as we observe that three-dimensional wakes exhibit a longer vortex formation region than the corresponding two-dimensional wake, as visualised in figure 13. Since a three-dimensional wake initially has a longer vortex formation region, it holds
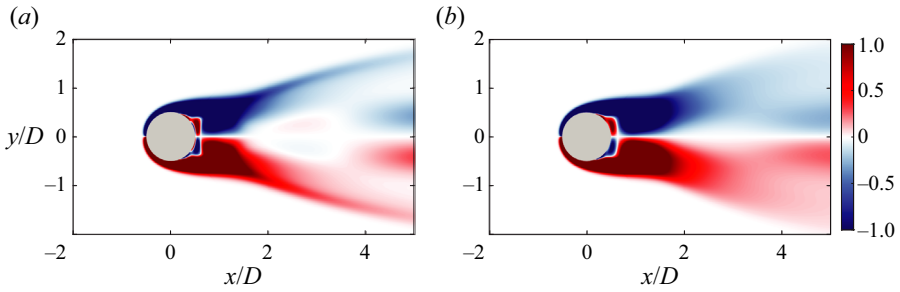
Figure 13. Contours of mean spanwise vorticity of the (*a*) two-dimensional and (*b*) three-dimensional wakes.
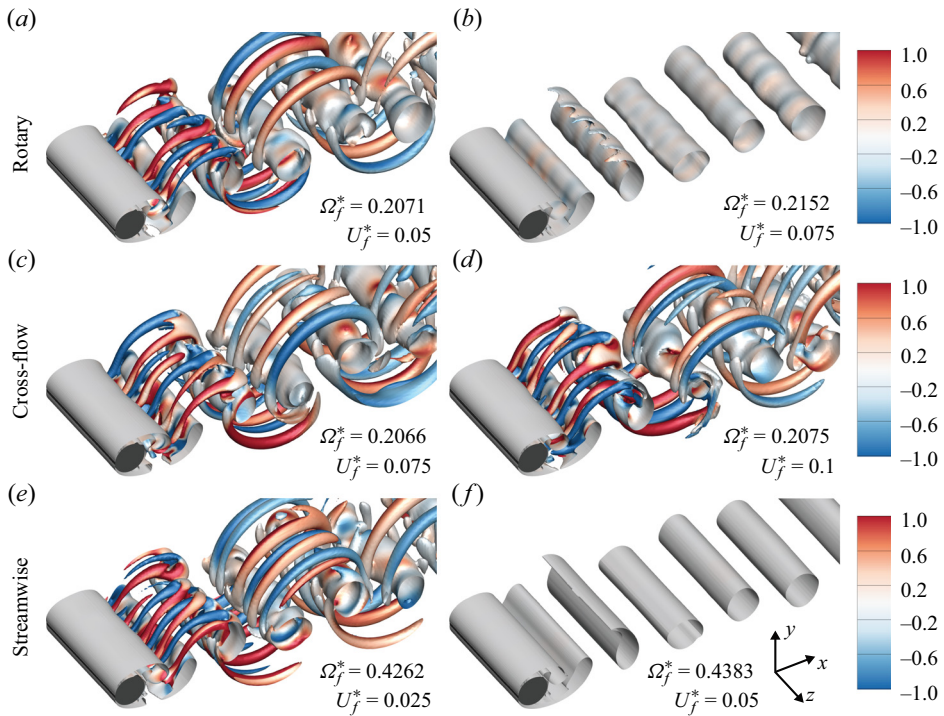

Figure 14. Wake visualisation with isosurfaces of the Q-criterion ($Q = 0.05$) coloured by ω_x for cases on the right synchronisation boundaries.

a greater capacity for shortening the vortex formation region. This offers an easier path to synchronisation for high-frequency oscillations in a three-dimensional wake compared with a two-dimensional wake, resulting in no inward deflection of the Arnold tongue at the right synchronisation boundary.

For the rotary oscillations, while the left synchronisation boundary agrees with the prediction, we find that the right synchronisation boundary of the three-dimensional wake obtained from DNS results deflects outward as the oscillation amplitude increases. This results in the three-dimensional wake having a larger upper bound than the two-dimensional wake when $U_f^* \geq 0.075$. Two instantaneous flow structures of cases on the right boundary with $U_f^* = 0.05$ and 0.075 for rotary motion are compared in figures 14(*a*) and 14(*b*). It is observed that secondary vortical structures disappear

1001 A24-20

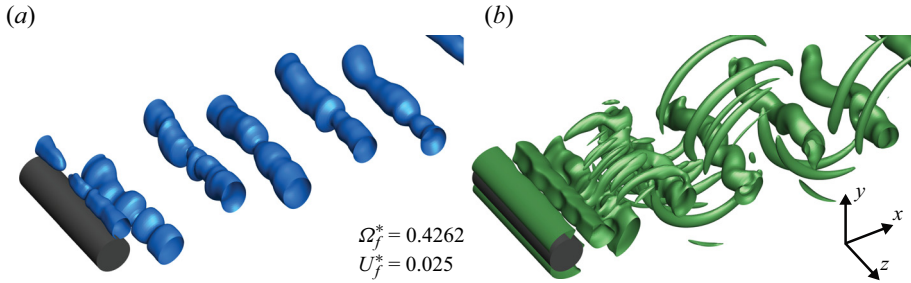(*a*)　　　　　　　　　　　　　　　　　(*b*)

$\Omega_f^* = 0.4262$
$U_f^* = 0.025$

Figure 15. Scale-decomposed flow structures by isosurfaces of the Q-criterion ($Q = 0.05$) corresponding to streamwise oscillation with $U_f^* = 0.025$ and $\Omega_f^* = 0.4262$ on the right synchronisation boundary: (*a*) large-scale structures and (*b*) small-scale structures.

when $U_f^* \geq 0.075$, showing that high-frequency rotary oscillations largely suppress the three-dimensionality of the wake. The suppression of secondary instabilities and the two-dimensionalisation of the wake by oscillatory cylinder motion are observed in previous studies as well (Poncet 2002; Deng, Shao & Ren 2007; Kim *et al.* 2009). This demonstrates the existence of a transition from a three-dimensional to a two-dimensional wake as the oscillation amplitude increases along the right branch. Due to this transition, cylinder wakes with high-frequency rotary oscillation deviate significantly from the unperturbed three-dimensional wake, which gives rise to the strong nonlinear response. Since phase reduction analysis adopts a first-order approximation to estimate the phase-sensitivity function, these nonlinear effects and the transition from a three-dimensional flow to a two-dimensional flow are not captured and are attributed to higher-order effects. On the other hand, such an outward deflection is not observed at the right boundary for cross-flow oscillations since the wake transition does not occur for this type of motion as shown in figure 14(*c*) and 14(*d*).

Regardless of the oscillation amplitude, the DNS-based right synchronisation boundary of the three-dimensional wake is always outside of the two-dimensional wake for the streamwise oscillations. Similar to the rotary oscillations, streamwise oscillations with $U_f^* = 0.05$ are able to two-dimensionalise the cylinder wake, while the three-dimensionality still remains at the oscillation amplitude of $U_f^* = 0.025$, shown in figure 14(*e*) and 14(*f*). To identify differences between the wakes and understand this observation further, we additionally examine scale-decomposed flow structures for this case on the right boundary, plotted in figure 15, and compare them with the unperturbed three-dimensional wakes provided in figure 4. We find that both large- and small-scale structures resemble the unperturbed three-dimensional wake with large r. This indicates that the three-dimensionality of the wake can be partially suppressed by the streamwise oscillation even though the oscillation amplitude is small. Due to the stronger nonlinear response of the wake to the streamwise motion, discrepancies between the synchronisation boundaries of the DNS results and the phase-reduction analysis can be large for this type of oscillation.

5. Conclusions

We have examined the influence of the three-dimensionality of the wake on its ability to synchronise to cylinder oscillations at $Re = 300$. Phase-reduction analysis was used for the theoretical analysis of wake synchronisation. Even though the ability of phase-reduction analysis to study the synchronisation of two-dimensional flows has been shown in previous

studies, the chaotic nature of three-dimensional wakes makes its implementation for these realistic flows challenging. To address this difficulty, we introduced an ensemble-averaging technique to extend phase-reduction analysis to three-dimensional flows. In addition, we provided a guideline to perform the ensemble-averaged phase-reduction analysis based on the direct method, which includes sample cycle extractions and measurements of phase-sensitivity functions. We applied phase-reduction analysis to both two- and three-dimensional cylinder wakes to understand the effect of three-dimensionality on synchronisation.

While the behaviour of the phase-sensitivity functions for two- and three-dimensional wakes are similar, due to two-dimensional von Kármán vortex shedding being the dominant feature in the wake dynamics of both, there is still a significant decrease in the phase-sensitivity of three-dimensional wake. This decrease is especially large for the cross-flow and rotary cylinder motions. This ultimately leads to reduced synchronisability and results in narrower Arnold tongues compared with the two-dimensional wake cases. Observing the amplitude variations from impulsive motions, the reduction of synchronisability was attributed to the energy transferred to the wake partially going into the amplitude direction. We have identified that the synchronisation conditions derived by phase-reduction analysis are valid for cylinder oscillations with velocities that are smaller than 10 % of the free-stream velocity. In addition, the parametric examination showed that there exists a minimum required oscillation amplitude to overcome the phase diffusion of the three-dimensional wake and achieve synchronisation. Nonlinear effects from wake three-dimensionality, which are associated with the vortex formation and transition from three- to two-dimensional flow, are also identified by analysing flow structures of synchronised wakes. To sum up, the phase-reduction analysis predicts the synchronisation conditions with reasonable accuracy, especially for small oscillation amplitudes when nonlinear effects are fairly small.

The present study has not only revealed synchronisation conditions of the three-dimensional cylinder wake but has also provided a systematic way to predict and analyse the synchronisation characteristics of more complex flows. Previous experimental studies observed that turbulent cylinder wakes at high Reynolds numbers (up to $Re \sim 10^5$) also exhibit rhythmic behaviours with a single dominant frequency, according to their energy spectrum, similar to the low-Reynolds-number wakes (Szepessy & Bearman 1992; Braza, Perrin & Hoarau 2006). Therefore, it is anticipated that phase characterisation of the flow is still valid, and the ensemble-based phase-reduction framework would be applicable, to turbulent flows with a high Reynolds number. Considering the sizable computational costs or experimental resources required to perform parametric studies, phase-reduction analysis gives an effective prediction of the synchronisation with reasonable precision.

1001 A24-22

Author ORCIDs.

- Youngjae Kim https://orcid.org/0009-0009-3915-9039;
- Vedasri Godavarthi https://orcid.org/0000-0002-1251-3343;
- Laura Victoria Rolandi https://orcid.org/0000-0003-1257-1102;
- Joseph T. Klamo https://orcid.org/0000-0003-1458-0379;
- Kunihiko Taira https://orcid.org/0000-0002-3762-8075.

REFERENCES

AL-MDALLAL, Q.M., LAWRENCE, K.P. & KOCABIYIK, S. 2007 Forced streamwise oscillations of a circular cylinder: locked-on modes and resulting fluid forces. *J. Fluids Struct.* **23** (5), 681–701.

BARKLEY, D. & HENDERSON, R.D. 1996 Three-dimensional Floquet stability analysis of the wake of a circular cylinder. *J. Fluid Mech.* **322**, 215–241.

BEARMAN, P.W. 1984 Vortex shedding from oscillating bluff bodies. *Annu. Rev. Fluid Mech.* **16** (1), 195–222.

BOWMAN, A.W. & AZZALINI, A. 1997 *Applied Smoothing Techniques for Data Analysis: The Kernel Approach with S-Plus Illustrations*. Oxford University Press.

BRAZA, M., PERRIN, R. & HOARAU, Y. 2006 Turbulence properties in the cylinder wake at high Reynolds numbers. *J. Fluids Struct.* **22** (6–7), 757–771.

CELIK, B. & BESKOK, A. 2009 Mixing induced by a transversely oscillating circular cylinder in a straight channel. *Phys. Fluids* **21** (7), 073601.

DENG, J., SHAO, X. & REN, A. 2007 Vanishing of three-dimensionality in the wake behind a rotationally oscillating circular cylinder. *J. Hydrodyn.* **19** (6), 751–755.

ERMENTROUT, G.B. & TERMAN, D.H. 2010 *Mathematical Foundations of Neuroscience*. Springer.

FUJINO, J., MOTOORI, Y. & GOTO, S. 2023 Hierarchy of coherent vortices in turbulence behind a cylinder. *J. Fluid Mech.* **975**, A13.

FUKAMI, K., NAKAO, H. & TAIRA, K. 2024 Data-driven transient lift attenuation for extreme vortex gust–airfoil interactions. *J. Fluid Mech.* **992**, A17.

GAU, C., WU, S.X. & SU, H.S. 2001 Synchronization of vortex shedding and heat transfer enhancement over a heated cylinder oscillating with small amplitude in streamwise direction. *Trans. ASME J. Heat Transfer* **123** (6), 1139–1148.

GODAVARTHI, V., KAWAMURA, Y. & TAIRA, K. 2023 Optimal waveform for fast synchronization of airfoil wakes. *J. Fluid Mech.* **976**, R1.

HAM, F. & IACCARINO, G. 2004 Energy conservation in collocated discretization schemes on unstructured meshes. *Annu. Res. Briefs* **2004**, 3–14.

HAM, F., MATTSSON, K. & IACCARINO, G. 2006 Accurate and stable finite volume operators for unstructured flow solvers. *Annu. Res. Briefs* **2006**, 243–261.

IIMA, M. 2019 Jacobian-free algorithm to calculate the phase sensitivity function in the phase reduction theory and its applications to Kármán's vortex street. *Phys. Rev.* E **99** (6), 062203.

IMAI, T., SUETANI, H. & AOYAGI, T. 2022 On the phase description of chaotic oscillators. *J. Phys. Soc. Japan* **91** (1), 014001.

JACKSON, C.P. 1987 A finite-element study of the onset of vortex shedding in flow past variously shaped bodies. *J. Fluid Mech.* **182**, 23–45.

JACONO, D.L., LEONTINI, J.S., THOMPSON, M.C. & SHERIDAN, J. 2010 Modification of three-dimensional transition in the wake of a rotationally oscillating cylinder. *J. Fluid Mech.* **643**, 349–362.

JIANG, H., CHENG, L., DRAPER, S., AN, H. & TONG, F. 2016 Three-dimensional direct numerical simulation of wake transitions of a circular cylinder. *J. Fluid Mech.* **801**, 353–391.

JOSIĆ, K. & MAR, D.J. 2001 Phase synchronization of chaotic systems with small phase diffusion. *Phys. Rev.* E **64** (5), 056234.

KAWAMURA, Y., GODAVARTHI, V. & TAIRA, K. 2022 Adjoint-based phase reduction analysis of incompressible periodic flows. *Phys. Rev. Fluids* **7** (10), 104401.

KHODKAR, M.A., KLAMO, J.T. & TAIRA, K. 2021 Phase-locking of laminar wake to periodic vibrations of a circular cylinder. *Phys. Rev. Fluids* **6** (3), 034401.

KHODKAR, M.A. & TAIRA, K. 2020 Phase-synchronization properties of laminar cylinder wake for periodic external forcings. *J. Fluid Mech.* **904**, R1.

KIM, J. & MOIN, P. 1985 Application of a fractional-step method to incompressible Navier–Stokes equations. *J. Comput. Phys.* **59** (2), 308–323.

KIM, S.H., PARK, J.Y., PARK, N., BAE, J.H. & YOO, J.Y. 2009 Direct numerical simulation of vortex synchronization due to small perturbations. *J. Fluid Mech.* **634**, 61–90.

KONSTANTINIDIS, E. & BOURIS, D. 2016 Vortex synchronization in the cylinder wake due to harmonic and non-harmonic perturbations. *J. Fluid Mech.* **804**, 248–277.

KRAVCHENKO, A.G., MOIN, P. & SHARIFF, K. 1999 B-spline method and zonal grids for simulations of complex turbulent flows. *J. Comput. Phys.* **151** (2), 757–789.

KUMAR, S., LOPEZ, C., PROBST, O., FRANCISCO, G., ASKARI, D. & YANG, Y. 2013 Flow past a rotationally oscillating cylinder. *J. Fluid Mech.* **735**, 307–346.

KUMAR, S., NAVROSE & MITTAL, S. 2016 Lock-in in forced vibration of a circular cylinder. *Phys. Fluids* **28** (11), 113605.

KURAMOTO, Y. 2003 *Chemical Oscillations, Waves, and Turbulence*. Dover.

KUREBAYASHI, W., FUJIWARA, K., NAKAO, H. & IKEGUCHI, T. 2012 A theory on noise-induced synchronization of chaotic oscillators. *IEICE Proc. Ser.* **1** (344), 344–347.

LEONTINI, J.S., JACONO, D.L. & THOMPSON, M.C. 2011 A numerical study of an inline oscillating cylinder in a free stream. *J. Fluid Mech.* **688**, 551–568.

LEONTINI, J.S., JACONO, D.L. & THOMPSON, M.C. 2013 Wake states and frequency selection of a streamwise oscillating cylinder. *J. Fluid Mech.* **730**, 162–192.

LEONTINI, J.S, JACONO, D.L. & THOMPSON, M.C. 2015 Stability analysis of the elliptic cylinder wake. *J. Fluid Mech.* **763**, 302–321.

LOE, I.A., NAKAO, H., JIMBO, Y. & KOTANI, K. 2021 Phase-reduction for synchronization of oscillating flow by perturbation on surrounding structure. *J. Fluid Mech.* **911**, R2.

LOE, I.A., ZHENG, T., KOTANI, K. & JIMBO, Y. 2023 Controlling fluidic oscillator flow dynamics by elastic structure vibration. *Sci. Rep.* **13** (1), 8852.

MARZOUK, O.A. & NAYFEH, A.H. 2009 Reduction of the loads on a cylinder undergoing harmonic in-line motion. *Phys. Fluids* **21** (8), 083103.

NAIR, A.G., TAIRA, K., BRUNTON, B.W. & BRUNTON, S.L. 2021 Phase-based control of periodic flows. *J. Fluid Mech.* **927**, A30.

NAKAO, H. 2016 Phase reduction approach to synchronisation of nonlinear oscillators. *Contemp. Phys.* **57** (2), 188–214.

NAUDASCHER, E. & ROCKWELL, D. 2005 *Flow-Induced Vibrations: An Engineering Guide*. Dover.

OLINGER, D.J. & SREENIVASAN, K.R. 1988 Nonlinear dynamics of the wake of an oscillating cylinder. *Phys. Rev. Lett.* **60** (9), 797.

ONGOREN, A. & ROCKWELL, D. 1988 Flow structure from an oscillating cylinder. Part 1. Mechanisms of phase shift and recovery in the near wake. *J. Fluid Mech.* **191**, 197–223.

PERDIKARIS, P.G., KAIKTSIS, L. & TRIANTAFYLLOU, G.S. 2009 Chaos in a cylinder wake due to forcing at the Strouhal frequency. *Phys. Fluids* **21** (10), 101705.

PERSILLON, H. & BRAZA, M. 1998 Physical analysis of the transition to turbulence in the wake of a circular cylinder by three-dimensional Navier–Stokes simulation. *J. Fluid Mech.* **365**, 23–88.

PIETRAS, B. & DAFFERTSHOFER, A. 2019 Network dynamics of coupled oscillators and phase reduction techniques. *Phys. Rep.* **819**, 1–105.

PIKOVSKY, A.S., ROSENBLUM, M.G., OSIPOV, G.V. & KURTHS, J. 1997 Phase synchronization of chaotic oscillators by external driving. *Physica* D **104** (3–4), 219–238.

PONCET, P. 2002 Vanishing of mode B in the wake behind a rotationally oscillating circular cylinder. *Phys. Fluids* **14** (6), 2021–2023.

PONTA, F.L. & AREF, H. 2005 Vortex synchronization regions in shedding from an oscillating cylinder. *Phys. Fluids* **17** (1), 011703.

POSDZIECH, O. & GRUNDMANN, R. 2001 Numerical simulation of the flow around an infinitely long circular cylinder in the transition regime. *Theor. Comput. Fluid Dyn.* **15** (2), 121–141.

PROVANSAL, M., MATHIS, C. & BOYER, L. 1987 Bénard-von Kármán instability: transient and forced regimes. *J. Fluid Mech.* **182**, 1–22.

ROLANDI, L.V., FONTANE, J., JARDIN, T., GRESSIER, J. & JOLY, L. 2023 Compressibility effects on the secondary instabilities of the circular cylinder wake. *J. Fluid Mech.* **966**, A36.

ROSENBLUM, M.G., PIKOVSKY, A.S. & KURTHS, J. 1996 Phase synchronization of chaotic oscillators. *Phys. Rev. Lett.* **76** (11), 1804.

SARPKAYA, T. 2004 A critical review of the intrinsic nature of vortex-induced vibrations. *J. Fluids Struct.* **19** (4), 389–447.

SCHWABEDAL, J.T.C., PIKOVSKY, A., KRALEMANN, B. & ROSENBLUM, M. 2012 Optimal phase description of chaotic oscillators. *Phys. Rev.* E **85** (2), 026216.

SHIOGAI, Y., STEFANOVSKA, A. & MCCLINTOCK, P.V.E. 2010 Nonlinear dynamics of cardiovascular ageing. *Phys. Rep.* **488** (2–3), 51–110.

SZEPESSY, S. & BEARMAN, P.W. 1992 Aspect ratio and end plate effects on vortex shedding from a circular cylinder. *J. Fluid Mech.* **234**, 191–217.

TAIRA, K. & NAKAO, H. 2018 Phase-response analysis of synchronization for periodic flows. *J. Fluid Mech.* **846**, R2.

TÖNJES, R. & KORI, H. 2022 Phase and frequency linear response theory for hyperbolic chaotic oscillators. *Chaos* **32** (4), 043124.

WANG, J., GENG, L., DING, L., ZHU, H. & YURCHENKO, D. 2020 The state-of-the-art review on energy harvesting from flow-induced vibrations. *Appl. Energy* **267**, 114902.

WILLIAMSON, C.H.K. 1996 Three-dimensional wake transition. *J. Fluid Mech.* **328**, 345–407.

WILLIAMSON, C.H.K. & GOVARDHAN, R. 2004 Vortex-induced vibrations. *Annu. Rev. Fluid Mech.* **36**, 413–455.

WILLIAMSON, C.H.K. & ROSHKO, A. 1988 Vortex formation in the wake of an oscillating cylinder. *J. Fluids Struct.* **2** (4), 355–381.

WINFREE, A.T. 1967 Biological rhythms and the behavior of populations of coupled oscillators. *J. Theor. Biol.* **16** (1), 15–42.

WOO, H.G.C. 1999 A note on phase-locked states at low Reynolds numbers. *J. Fluids Struct.* **13** (1), 153–158.

YASUDA, T., GOTO, S. & VASSILICOS, J.C. 2020 Formation of power-law scalings of spectra and multiscale coherent structures in the near-field of grid-generated turbulence. *Phys. Rev. Fluids* **5** (1), 014601.

ZHANG, H.-Q., FEY, U., NOACK, B.R., KÖNIG, M. & ECKELMANN, H. 1995 On the transition of the cylinder wake. *Phys. Fluids* **7** (4), 779–794.